Electronic Supplementary Material (ESI) for Physical Chemistry Chemical Physics.
This journal is © the Owner Societies 2020

Electronic Supplementary Information for

π-Orbital Yin-Yang Kagome Bands in Anilato-based Metal-organic Frameworks

Xiaojuan Ni, Yinong Zhou, Gurjyot Sethi, and Feng Liu*

Department of Materials Science and Engineering, University of Utah, Salt Lake City, Utah 84112, USA

*Corresponding author e-mail: fliu@eng.utah.edu

This Electronic Supplementary Information (ESI) contains computational methods, supporting figures, tables, and discussion.

Computational methods

The first-principles calculations for anilato-based MOFs were carried out in the framework of the Perdew-Burke-Ernzerhof (PBE) generalized gradient approximation functional using the Vienna ab initio simulation package (VASP).[1,2] All the self-consistent calculations were performed with a plane-wave cutoff of 500 eV on a 5×5×1 Monkhorst-Pack k-point mesh with the vacuum layer more than 15 Å thick to ensure the decoupling between the neighboring slabs. For the structural relaxation, all the atoms are allowed to relax until the atomic forces are smaller than 0.01 eV/ Å. The maximally localized Wannier functions (MLWFs) is employed to fit the DFT band structure.[3–5] The correction of van der Waals interaction (DFT-D2) is considered to calculate the binding energy. The screened hybrid functional of Heyd, Scuseria, and Ernzerhof (HSE)[6] is also employed to calculate band structures in order to have a more accurate estimation of the band gap. The molecular properties of benzene, chloranilic acid, other anilato-based molecules were calculated using Gaussian16 with B3LYP functional and 6-31G basis set.[7]

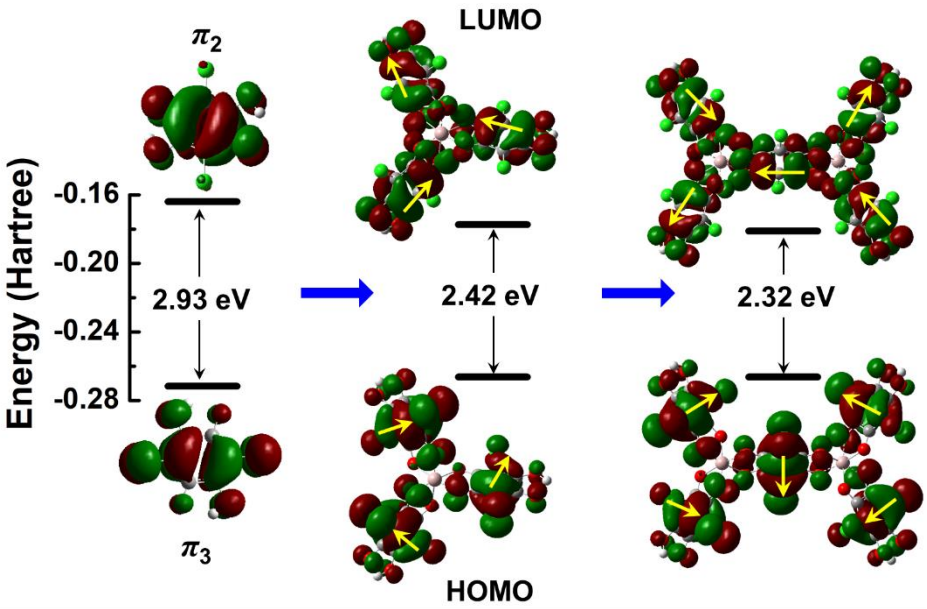

Figure S1. The LUMO and HOMO of monomer CLA, trimer with one Al ion, and pentamer with two Al ions. The green and red represent the positive and negative sign of lobes. The yellow arrow indicates the direction from positive to negative lobes across the nodal plane in π_2- and π_3-orbitals.

As shown in Fig. S1, starting with the CLA monomer, the LUMO and HOMO states have the features of π_2- and π_3-orbitals, respectively, and are separated with a gap of 2.93 eV. Note that the π_2- and π_3-orbitals are formed with C-O and C-Cl orbital hybridizations, with no or little contribution from Al and O orbitals, respectively. As such, the position of nodal line of π_2- and π_3-orbitals is simply defined by positions of Cl and O atom positions, while their relative energy positions are related to the chemical potential of Cl and O and the amount of charge transfer they draw from C. After binding with Al ions, the main features of these two states remain the same, except a reduced gap of 2.42 eV in the trimer with one Al ion and of 2.32 eV in a pentamer with two Al ions. Also, there is a phase change in the π-orbitals around each Al ion, as indicated by the yellow arrows.

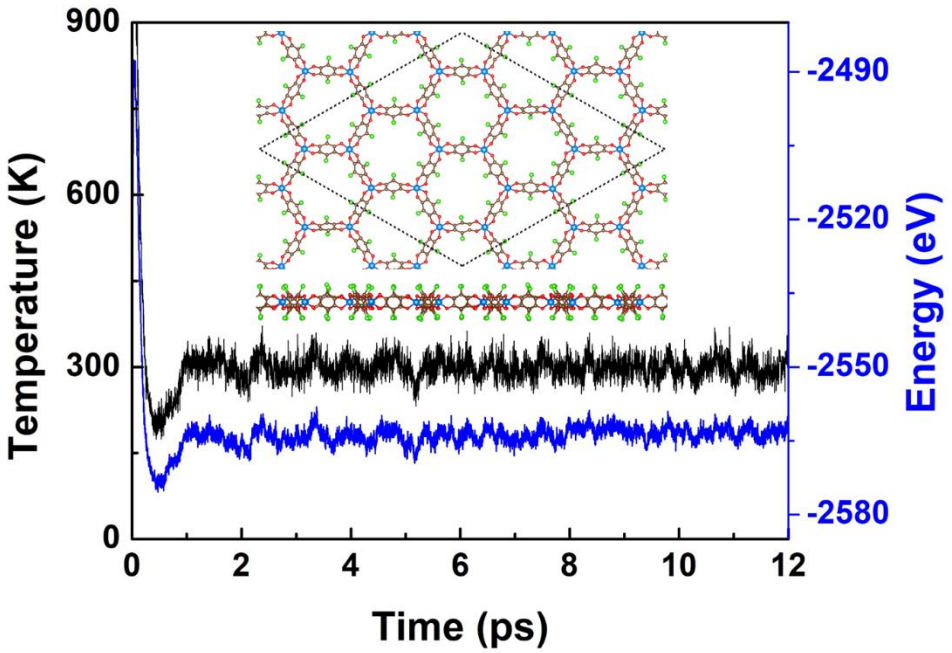

Figure S2. Temperature and energy fluctuations as a function of time from ab initio molecular dynamics simulation. The insets show the top and side views of monolayer $Al_2(C_6O_4Cl_2)_3$ at the end of simulation. The dashed rhombus indicates the supercell.

To examine the structural stability of MOF $Al_2(C_6O_4Cl_2)_3$, a 3×3 super cell containing 342 atoms was adopted to perform *ab initio* molecular dynamics simulations with the canonical ensemble (NVT) at 300 K. Figure S2 shows the evolution of temperature and total energy, and the insets show the top and side views of $Al_2(C_6O_4Cl_2)_3$ at the end of the simulation. No destruction was found in the framework up to 12 ps of simulation, confirming the stability of monolayer $Al_2(C_6O_4Cl_2)_3$ at room temperature.

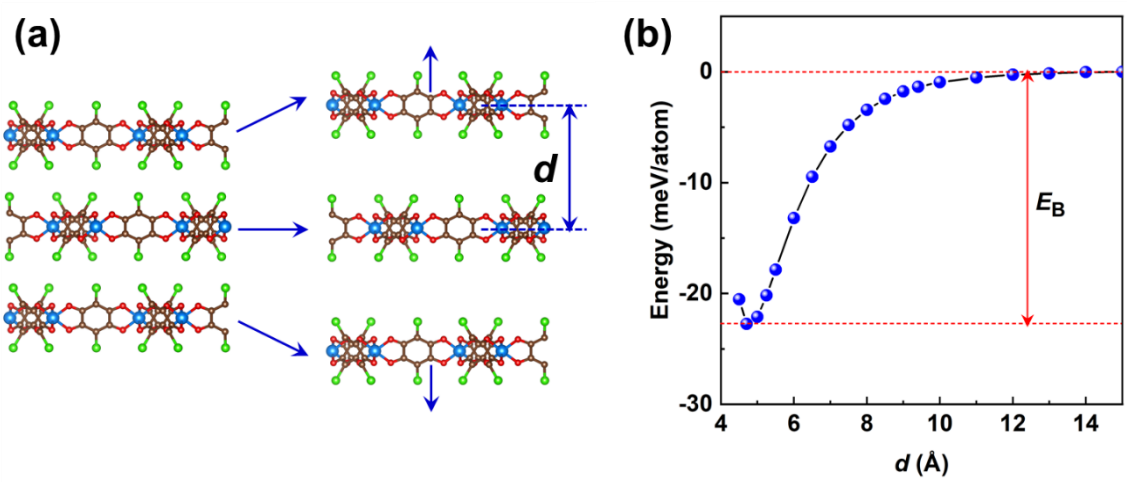

Figure S3. (a) Illustration of the structure of anilato-based MOFs with the increasing interlayer distance, *d*. (b) The energy as a function of interlayer distance, from which the interlayer binding energy, E_B is derived.

The interlayer binding energy in anilato-based MOFs has been calculated as a function of interlayer distance, d, as shown in Fig. S3(a). The experimentally observed AB stacking of bulk $Al_2(C_6O_4Cl_2)_3$ is adopted for the calculation including the correction of van der Waals interaction (DFT-D2). The relaxed layered bulk $Al_2(C_6O_4Cl_2)_3$ has the lattice constants of a = 13.14 and c = 9.41 Å. The binding energy, E_B, is derived to be ~23 meV/atom [Fig. S3(b)], which falls into the typical range of van der Waals interlayer strength, such as those in graphite and layered transition metal dichalcogenides[8,9]. This indicates a high feasibility of exfoliating layered anilato-based MOFs into 2D layers, similar to other 2D materials.

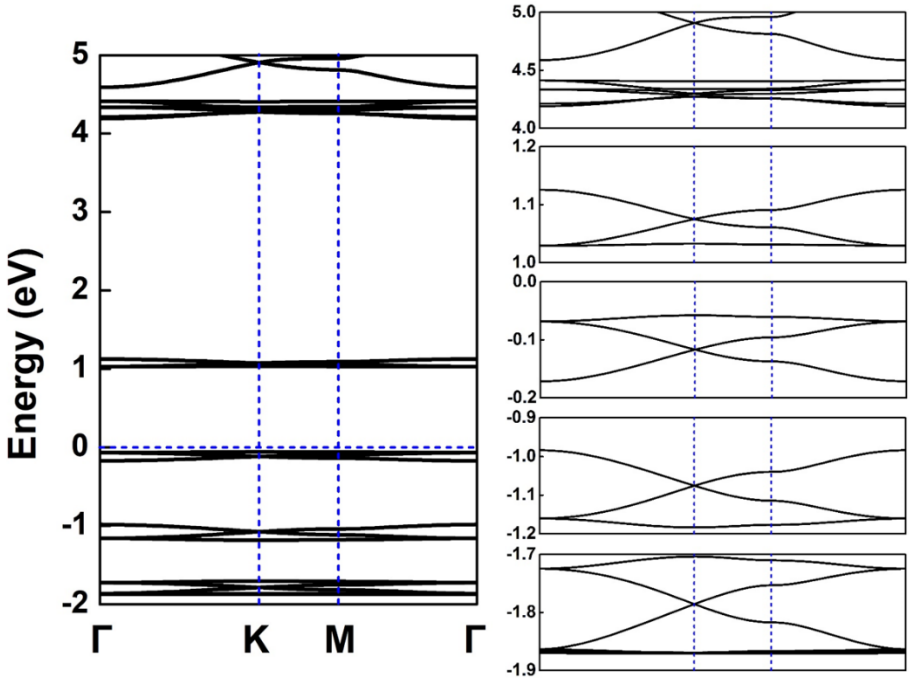

Figure S4. DFT band structure of $Al_2(C_6O_4Cl_2)_3$. Left panel shows the extended energy range beyond the Yin-Yang Kagome bands. Right panel shows the zoom-in band structures. The Yin-Yang Kagome bands are isolated from other bands in energy.

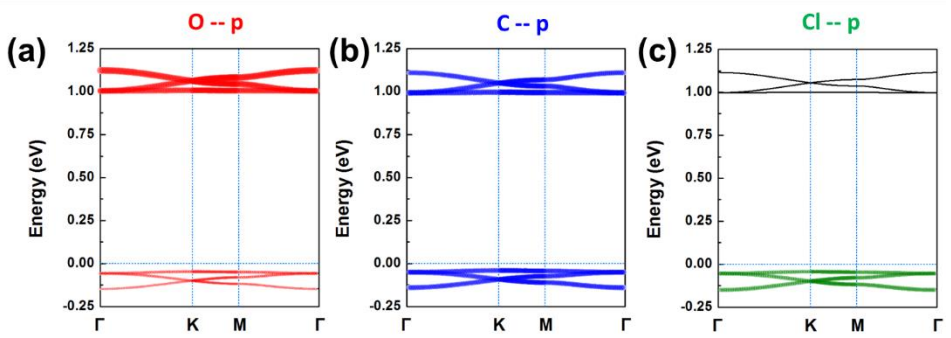

Figure S5. Band decomposition of $Al_2(C_6O_4Cl_2)_3$. The red, blue, and green represent the contribution from *p* orbitals of O, C, and Cl, respectively.

As shown in Fig. S5, the decomposed orbital contributions to each band indicate clearly that the valence Kagome bands mainly come from *p* orbitals of C and Cl atoms, while the conduction Kagome bands come from *p* orbitals of O and C atoms. These are consistent with the atomic orbital contributions to π_2- and π_3-orbitals of CLAs, as shown in Fig. 1(c), Fig. S1, and related discussions.

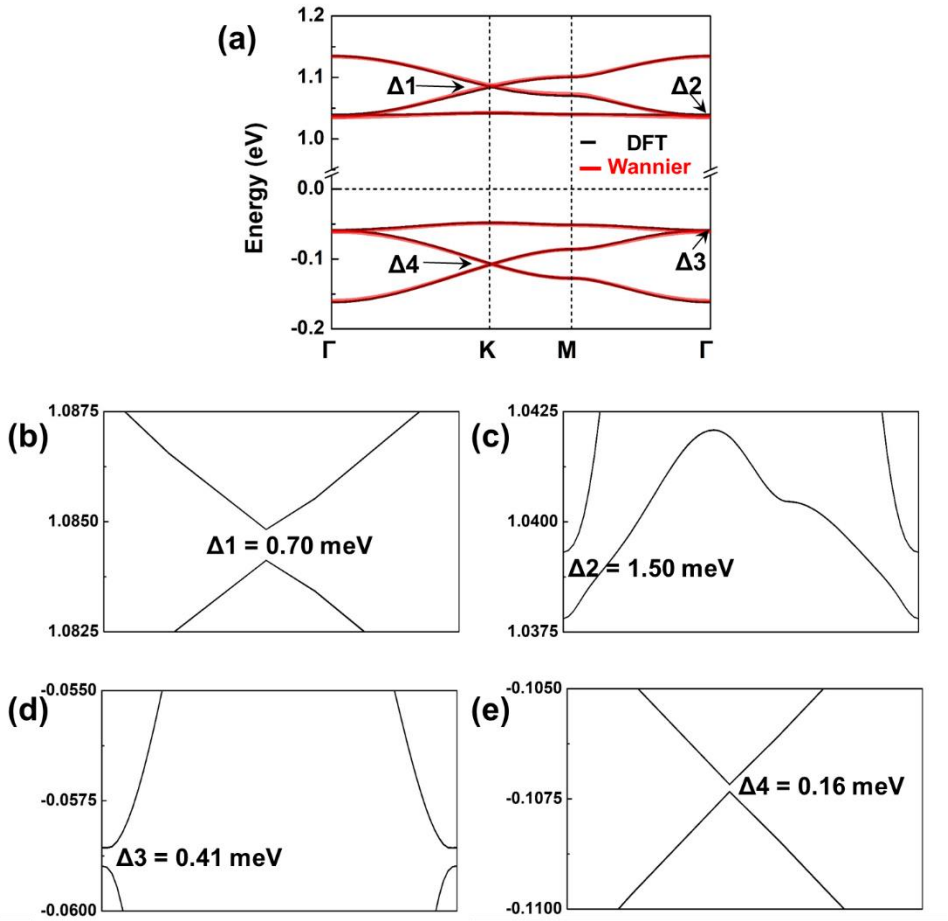

Figure S6. (a) First-principles (black) and Wannier (red) band structures of $Al_2(C_6O_4Cl_2)_3$. Δ1 and Δ2 indicate the gaps at *K* and *Γ* in conduction Kagome bands, and Δ3 and Δ4 indicate the gaps at *Γ* and *K* in valence Kagome bands, respectively. The zoom-in band structures around (b) Δ1, (c) Δ2, (d) Δ3, and (e) Δ4.

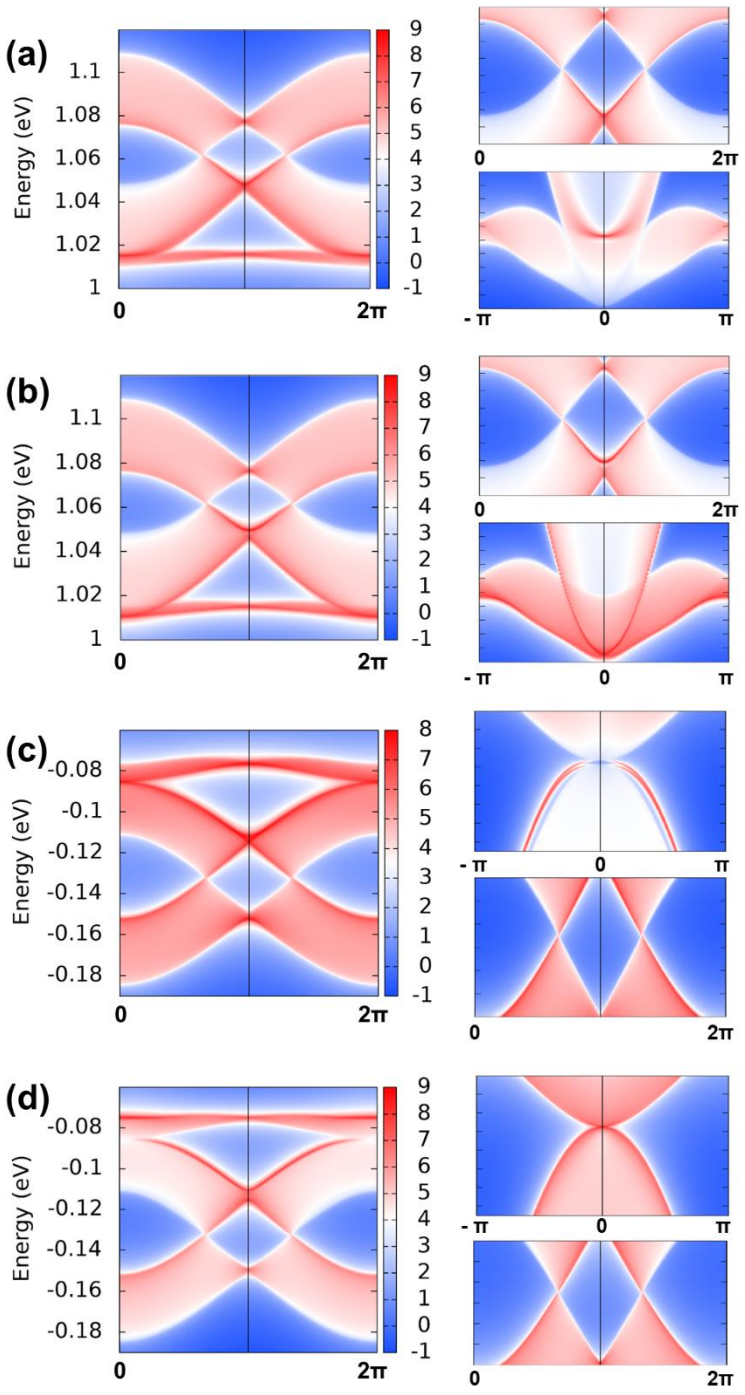

Figure S7. Edge states in $Al_2(C_6O_4Cl_2)_3$. Conduction Kagome bands: edge states with (a) right and (b) left terminations. Right panel shows the zoom-in edge states at *K* and *Γ* points. Valence Kagome bands: edge states with (a) right and (b) left terminations. Right panel shows the zoom-in edge states at *Γ* and *K* points.

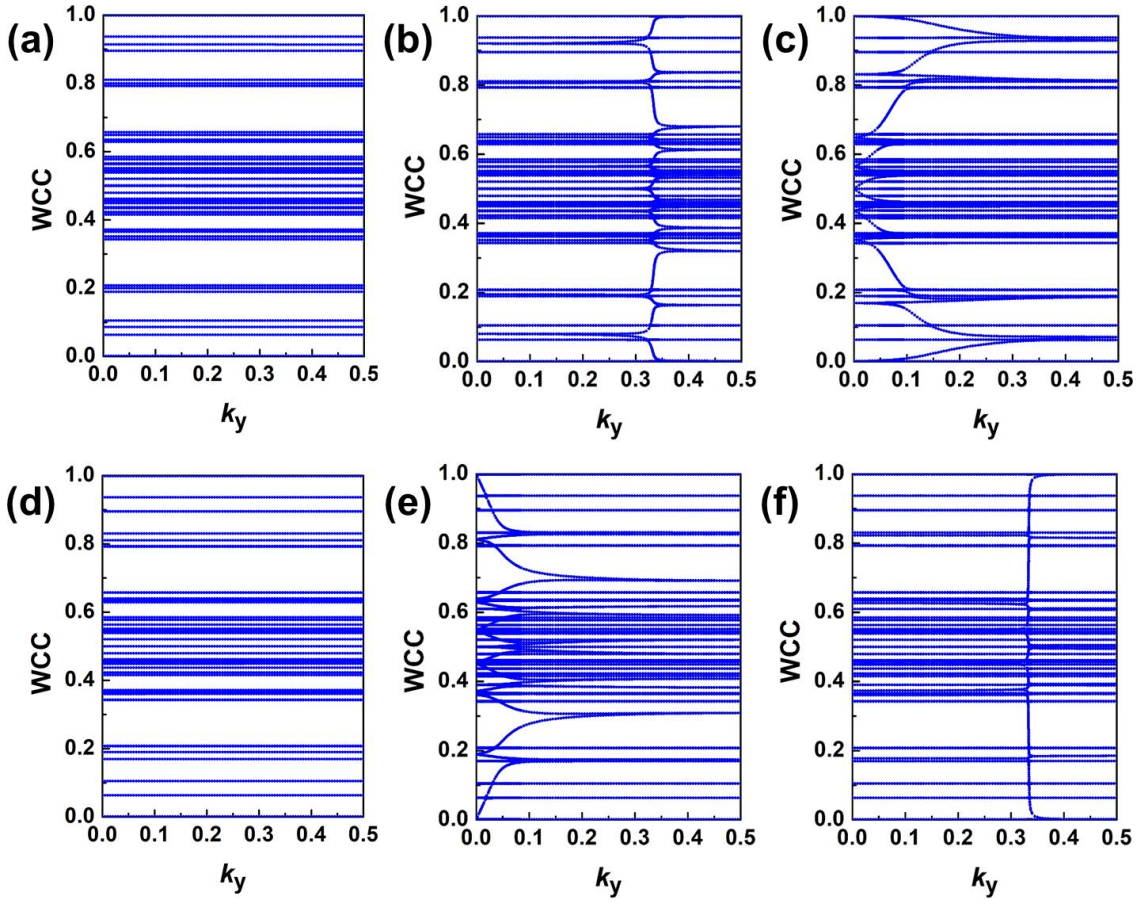

Figure S8. Wannier charge centers for the occupation up to (a) the top of enantiomorphic (Z_2 = 0) Kagome bands, and the gaps of (b) Δ1 (Z_2 = 1), (c) Δ2 (Z_2 = 1), (d) E_{g_FB} (Z_2 = 0), (d) Δ3 (Z_2 = 1), and (e) Δ4 (Z_2 = 1).

The TB Hamiltonian is,

$$H = H_\varepsilon + H_1 + H_2 + H_{SOC}$$

where $H\varepsilon$ is the on-site term, for one spin channel, it becomes

$$H_\varepsilon = \begin{pmatrix} \varepsilon_{\pi_2} & 0 & 0 & 0 & 0 & 0 \\ 0 & \varepsilon_{\pi_2} & 0 & 0 & 0 & 0 \\ 0 & 0 & \varepsilon_{\pi_2} & 0 & 0 & 0 \\ 0 & 0 & 0 & \varepsilon_{\pi_3} & 0 & 0 \\ 0 & 0 & 0 & 0 & \varepsilon_{\pi_3} & 0 \\ 0 & 0 & 0 & 0 & 0 & \varepsilon_{\pi_3} \end{pmatrix}.$$

H_1 is the NN hopping, $H_1 = \begin{pmatrix} H_{\pi_2}^1 & 0 \\ 0 & H_{\pi_3}^1 \end{pmatrix}$ with

$$H_{\pi_2}^1 = 2t_1^{\pi_2} \begin{pmatrix} 0 & \cos k_1 & -\cos k_2 \\ \cos k_1 & 0 & -\cos k_3 \\ -\cos k_2 & -\cos k_3 & 0 \end{pmatrix}, \text{ and}$$

$$H_{\pi_3}^1 = 2t_1^{\pi_3} \begin{pmatrix} 0 & -\cos k_1 & \cos k_2 \\ -\cos k_1 & 0 & \cos k_3 \\ \cos k_2 & \cos k_3 & 0 \end{pmatrix},$$

where k_n is defined as $k_n = \vec{k} \cdot \overrightarrow{a_n}$, and $\overrightarrow{a_1} = \left(\frac{\sqrt{3}}{2}\hat{x} + \frac{1}{2}\hat{y}\right)$, $\overrightarrow{a_2} = \left(\frac{\sqrt{3}}{2}\hat{x} - \frac{1}{2}\hat{y}\right)$, $\overrightarrow{a_3} = \hat{y}$.

H_{soc} is the SOC term, $H_{SOC} = \begin{pmatrix} H_{\pi_2}^{SOC} & 0 \\ 0 & H_{\pi_3}^{SOC} \end{pmatrix}$ with

$$H_{\pi_2}^{SOC} = i2\lambda_{SOC}^{\pi_2} \begin{pmatrix} 0 & -\cos(k_2 - k_3) & \cos(k_1 + k_3) \\ -\cos(k_2 - k_3) & 0 & -\cos(k_1 + k_2) \\ \cos(k_1 + k_3) & -\cos(k_1 + k_2) & 0 \end{pmatrix}, \text{ and}$$

$$H_{\pi_3}^{SOC} = i2\lambda_{SOC}^{\pi_3} \begin{pmatrix} 0 & -\cos(k_2 - k_3) & \cos(k_1 + k_3) \\ -\cos(k_2 - k_3) & 0 & -\cos(k_1 + k_2) \\ \cos(k_1 + k_3) & -\cos(k_1 + k_2) & 0 \end{pmatrix}.$$

The Chern number is defined as[10]

$$C = \frac{1}{2\pi} \int_{BZ} d^2k F_{12}(k)$$

where $F_{12}(k) = \frac{\partial}{\partial k_1} A_2(k) - \frac{\partial}{\partial k_2} A_1(k)$ is the associated field strength, $A_\mu(k) = -i \left\langle n_k \middle| \frac{\partial}{\partial k_\mu} \middle| n_k \right\rangle$ is the Berry connection, $|n_k\rangle$ is a normalized wave function of the respective band.

H_2 is the 2NN hopping, which reads as

$$H_2 = \begin{pmatrix} H_{\pi_2}^2 & 0 \\ 0 & H_{\pi_3}^2 \end{pmatrix} \text{ with}$$

$$H_{\pi_2}^2 = 2t_2^{\pi_2} \begin{pmatrix} 0 & -\cos(k_2 - k_3) & \cos(k_1 + k_3) \\ -\cos(k_2 - k_3) & 0 & \cos(k_1 + k_2) \\ \cos(k_1 + k_3) & \cos(k_1 + k_2) & 0 \end{pmatrix}, \text{ and}$$

$$H_{\pi_3}^2 = 2t_2^{\pi_3} \begin{pmatrix} 0 & \cos(k_2 - k_3) & -\cos(k_1 + k_3) \\ \cos(k_2 - k_3) & 0 & -\cos(k_1 + k_2) \\ -\cos(k_1 + k_3) & -\cos(k_1 + k_2) & 0 \end{pmatrix}.$$

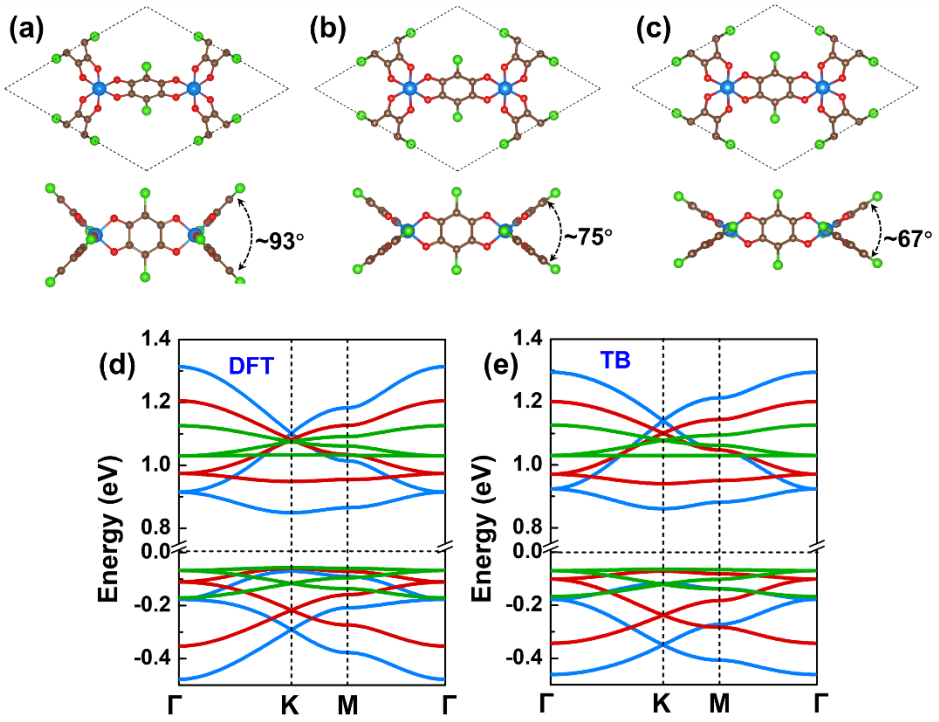

Figure S9. Top and auxiliary views of the crystal structures of $Al_2(C_6O_4Cl_2)_3$ for DA = 93° (a), 75° (b), and 67° (c). Band structures obtained from DFT calculations (d) and TB model (e) for DA = 67° (blue), 75° (red), and 93° (green), respectively.

Table S1. Parameters used in TB model to fit DFT band structures.

DA (°) / (eV)	93	75	67
$t_1^{\pi_2}$	0.016	0.044	0.072
$t_2^{\pi_2}$	0	0.005	0.0105
ε_{π_2}	1.062	1.047	1.047
$t_1^{\pi_3}$	0.017	0.045	0.057
$t_2^{\pi_3}$	0.0009	0.005	0.01
ε_{π_3}	-0.103	-0.183	-0.273

Considering SOC, the size of Hamiltonian is doubled. There are 12 bands in total in enantiomorphic Kagome bands with index of 1 to 12 from bottom to top. The Z_2 number is derived based on the parity at time-reversal invariant momenta, as listed in Table S2.

Table S2. The total parity at time-reversal invariant momenta, Γ and M points, and the Z_2 number with different occupation.

TRIM / Band#	Γ	M_1	M_2	M_3	Product	Occupation	Z_2
11,12	+	-	-	-	-1	all	**0**
9,10	+	+	+	+	+1	Δ1	**1**
7,8	+	-	-	-	-1	Δ2	**1**
5,6	+	-	-	-	-1	E_{g_FB}	**0**
3,4	+	+	+	+	+1	Δ3	**1**
1,2	+	-	-	-	-1	Δ4	**1**

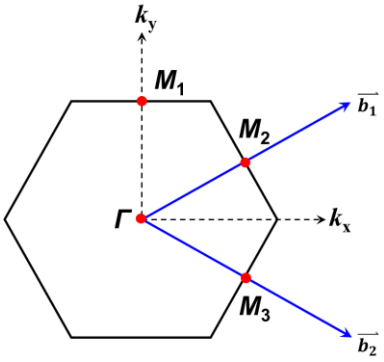

Figure S10. The first Brillouin zone of Kagome lattice. The points of Γ, M_1, M_2, and M_3 are time-reversal invariant momenta.

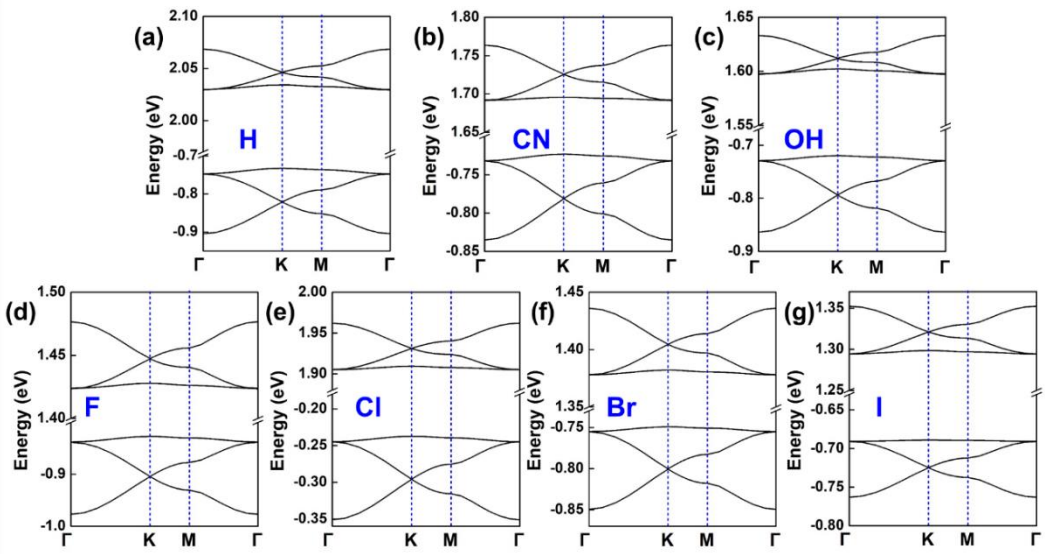

Figure S11. HSE06 band structures of $Al_2(C_6O_4X_2)_3$ with X = (a) H, (b) CN, (c) OH, (d) F, (e) Cl, (f) Br, and (g) I.

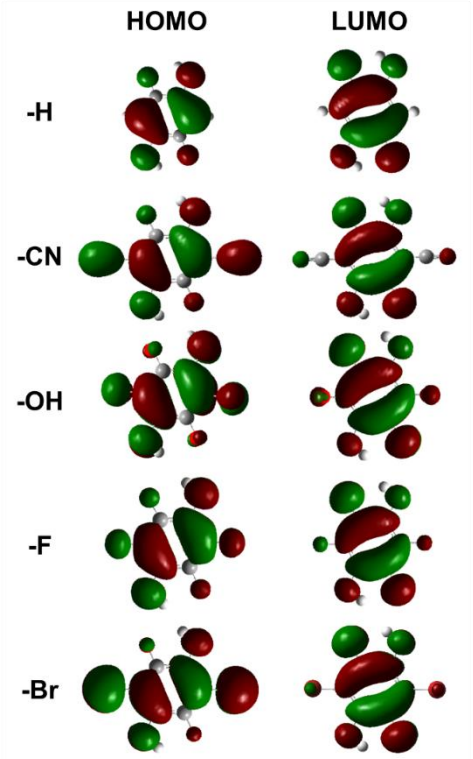

Figure S12. HOMO and LUMO in anilato-based molecule $C_6O_4X_2H_2$ with X = H, CN, OH, F, and Br, respectively. Green and red indicate the positive and negative sign of lobes, respectively.

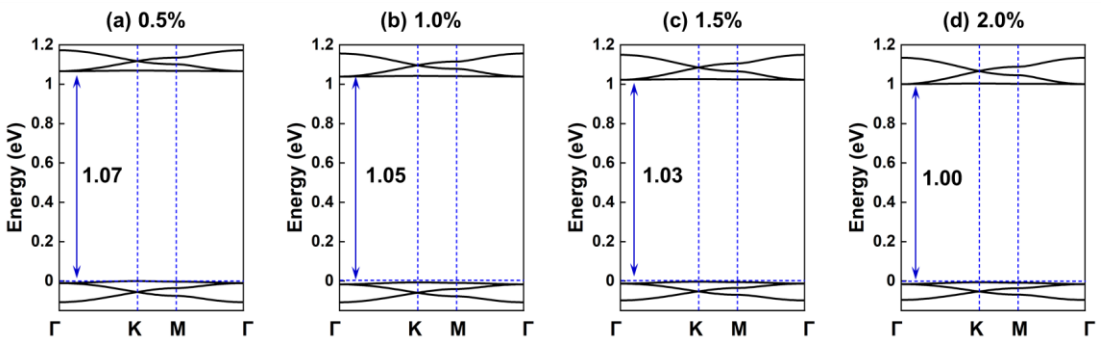

Figure S13. Band structures of $Al_2(C_6O_4Cl_2)_3$ under the strain of (a) 0.5%, (b) 1.0%, (c) 1.5%, and (d) 2.0%, respectively. The inset number indicates the band gap.

Up to 2.0% tensile strains, all the calculated $Al_2(C_6O_4Cl_2)_3$ MOFs still host the Yin-Yang Kagome bands, as shown in Fig. S13. The band gap decreases slightly with the increasing strain.

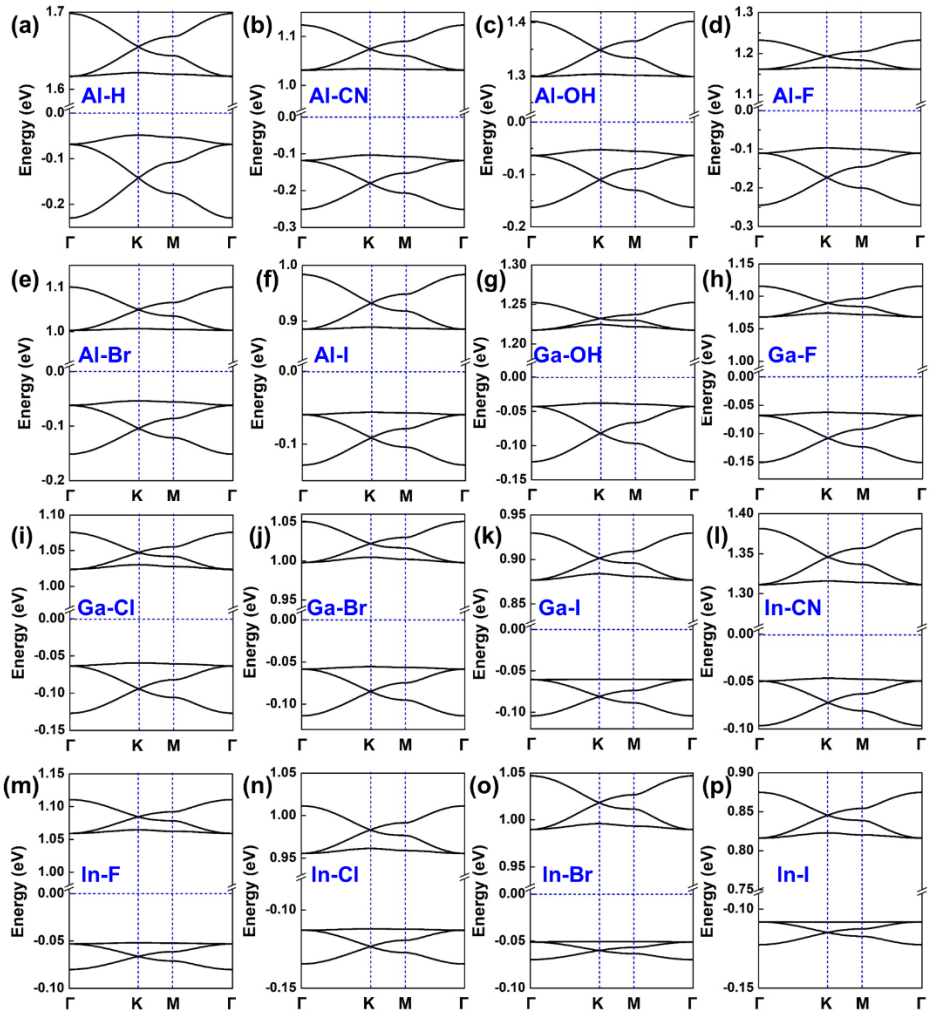

Figure S14. Band structures of $M_2(C_6O_4X_2)_3$ with M-X = (a) Al-H, (b) Al-CN,(c) Al-OH, (d) Al-F, (e) Al-Br, (f) Al-I, (g) Ga-OH, (h) Ga-F, (i) Ga-Cl, (j) Ga-Br, (k) Ga-I, (l) In-CN, (m) In-F, (n) In-Cl, (o) In-Br, and (p) In-I, respectively.

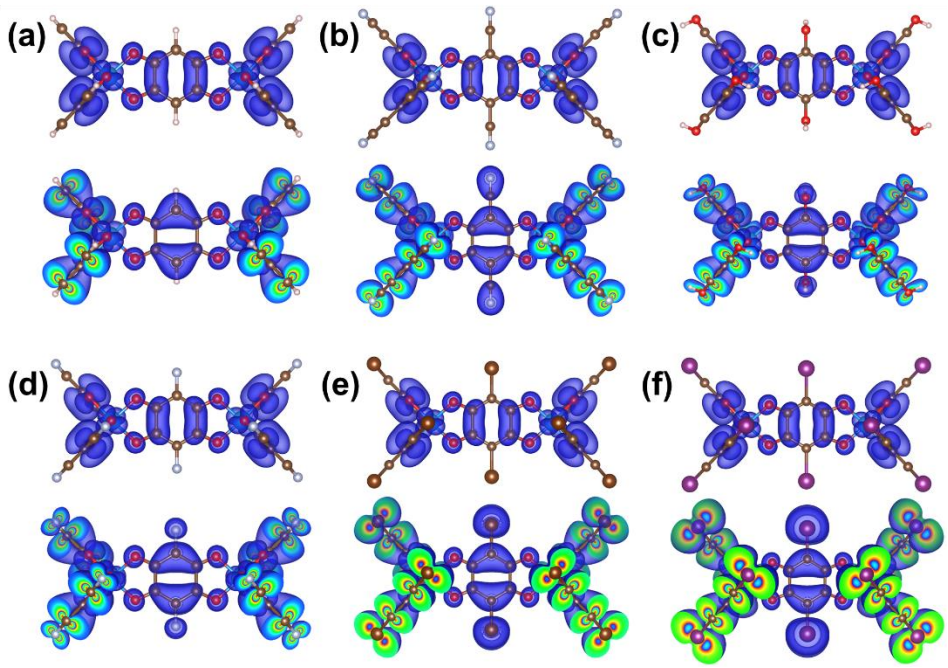

Figure S15. Partial charge distribution for $Al_2(C_6O_4X_2)_3$ with X = (a) H, (b) CN, (c) OH, (d) F, (e) Br, and (f) I. In each figure, top panel is for conduction Kagome bands and bottom panel is for valence Kagome bands, respectively.

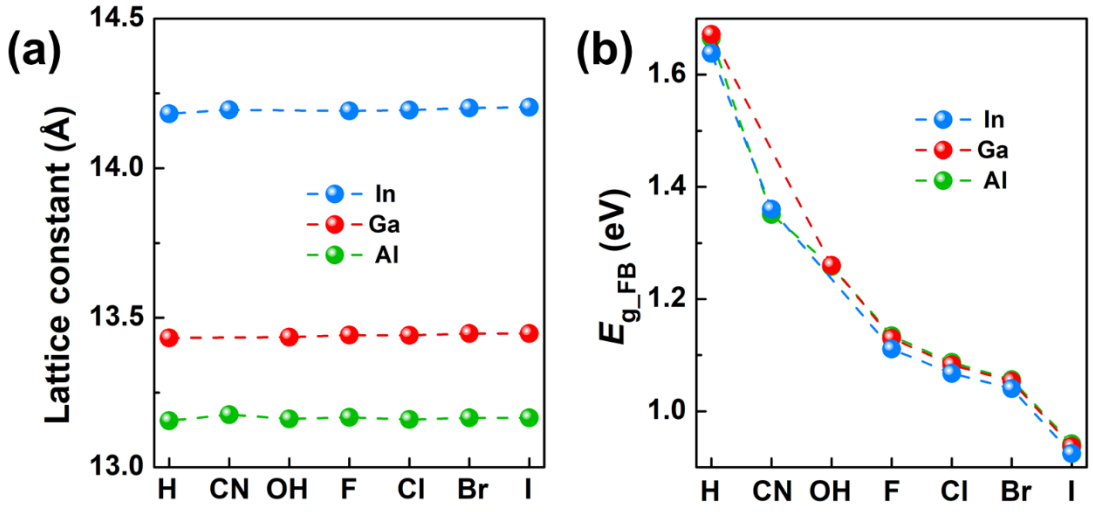

Figure S16. (a) lattice constant and (b) band gap between two FBs of $M_2(C_6O_4X_2)_3$ with X = H, CN, OH, F, Br, and I, and M = Al, Ga, and In, respectively.

References

1 G. Kresse and J. Furthmuller, *Phys. Rev. B*, 1996, **54**, 11169–11186.

2 J. P. Perdew, K. Burke and M. Ernzerhof, *Phys. Rev. Lett.*, 1996, **77**, 3865–3868.

3 A. A. Mostofi, J. R. Yates, Y. Lee, I. Souza, D. Vanderbilt and N. Marzari, *Comput. Phys. Commun.*, 2008, **178**, 685–699.

4 I. Souza, N. Marzari and D. Vanderbilt, *Phys. Rev. B - Condens. Matter Mater. Phys.*, 2002, **65**, 035109.

5 N. Marzari and D. Vanderbilt, *Phys. Rev. B - Condens. Matter Mater. Phys.*, 1997, **56**, 12847–12865.

6 A. V. Krukau, O. A. Vydrov, A. F. Izmaylov and G. E. Scuseria, *J. Chem. Phys.*, , DOI:10.1063/1.2404663.

7 M. J. Frisch, G. W. Trucks, H. B. Schlegel, G. E. Scuseria, M. A. Robb, J. R. Cheeseman, G. Scalmani, V. Barone, G. A. Petersson, H. Nakatsuji, X. Li, M. Caricato, A. V Marenich, J. Bloino, B. G. Janesko, R. Gomperts, B. Mennucci, H. P. Hratchian, J. V Ortiz, A. F. Izmaylov, J. L. Sonnenberg, D. Williams-Young, F. Ding, F. Lipparini, F. Egidi, J. Goings, B. Peng, A. Petrone, T. Henderson, D. Ranasinghe, V. G. Zakrzewski, J. Gao, N. Rega, G. Zheng, W. Liang, M. Hada, M. Ehara, K. Toyota, R. Fukuda, J. Hasegawa, M. Ishida, T. Nakajima, Y. Honda, O. Kitao, H. Nakai, T. Vreven, K. Throssell, J. A. Montgomery Jr., J. E. Peralta, F. Ogliaro, M. J. Bearpark, J. J. Heyd, E. N. Brothers, K. N. Kudin, V. N. Staroverov, T. A. Keith, R. Kobayashi, J. Normand, K. Raghavachari, A. P. Rendell, J. C. Burant, S. S. Iyengar, J. Tomasi, M. Cossi, J. M. Millam, M. Klene, C. Adamo, R. Cammi, J. W. Ochterski, R. L. Martin, K. Morokuma, O. Farkas, J. B. Foresman and D. J. Fox, 2016.

8 T. Björkman, A. Gulans, A. V. Krasheninnikov and R. M. Nieminen, *Phys. Rev. Lett.*, 2012, **108**, 235502.

9 N. Mounet, M. Gibertini, P. Schwaller, D. Campi, A. Merkys, A. Marrazzo, T. Sohier, I. E. Castelli, A. Cepellotti, G. Pizzi and N. Marzari, *Nat. Nanotechnol.*, 2018, **13**, 246–252.

10 D. J. Thouless, M. Kohmoto, M. P. Nightingale and M. den Nijs, *Phys. Rev. Lett.*, 1982, **49**, 405–408.